# Study on the Shape of Staggered Electrodes for 3-D Electrical Capacitance Tomography Sensors

Jingjing Shen<sup>®</sup>, Shuanghe Meng<sup>®</sup>, Jing Wang<sup>®</sup>, Wuqiang Yang<sup>®</sup>, Fellow, IEEE, and Mao Ye<sup>®</sup>

Abstract—A conventional electrical capacitance tomography (ECT) sensor consists of multiple rectangular electrodes in a single plane. To generate 3-D images, some researchers use an ECT sensor with multiplane rectangular electrodes and in-line arrangement of different electrode planes and measure the capacitance between the electrode pairs not only within the same plane but also between different planes. Because those electrode pairs in different planes are far away from each other, the measured capacitance signals between them are weak and, hence, are easily affected by noise, resulting in the obvious disturbance on the measured signals and, hence, low image quality. To address those problems, the 3-D ECT sensors with different arrangements and different shapes of electrodes are studied to investigate the effect of different arrangements and different shapes of electrodes on the measured capacitance signals and the image quality. Four 3-D ECT sensors are made with different arrangements or shapes of electrodes: rectangular electrodes are in line arrangement, whereas diamond, circular, and hexagon electrodes are staggered arrangement. The performance of the four 3-D ECT sensors is compared. The results show that 3-D ECT sensors with staggered electrodes can decrease the disturbance on the measured signals and improve the image quality of static models compared with that with conventional rectangular electrodes. Among the three 3-D ECT sensors with staggered electrodes, the 3-D ECT sensor with hexagonal electrodes has superior performance to the other two 3-D ECT sensors with diamond and circular electrodes. It was used to measure moving objects and a fluidized bed.

*Index Terms*—3-D electrical capacitance tomography (ECT) sensor, electrode shape, image quality, measurement signal, staggered electrodes.

Manuscript received September 20, 2020; revised November 2, 2020; accepted November 15, 2020. Date of publication November 27, 2020; date of current version December 29, 2020. This work was supported in part by the National Key Research and Development Program of China under Grant 2018YFB0604904 and in part by the National Natural Science Foundation of China under Grant 91834302. The Associate Editor coordinating the review process was Chao Tan. (Corresponding author: Mao Ye.)

Jingjing Shen is with the Dalian National Laboratory for Clean Energy, Dalian Institute of Chemical Physics, Chinese Academy of Sciences, Dalian 116023, China, also with the National Engineering Laboratory for MTO, Dalian Institute of Chemical Physics, Chinese Academy of Sciences, Dalian 116023, China, and also with the University of Chinese Academy of Sciences, Beijing 100049, China (e-mail: shenjing@dicp.ac.cn).

Shuanghe Meng, Jing Wang, and Mao Ye are with the Dalian National Laboratory for Clean Energy, Dalian Institute of Chemical Physics, Chinese Academy of Sciences, Dalian 116023, China, and also with the National Engineering Laboratory for MTO, Dalian Institute of Chemical Physics, Chinese Academy of Sciences, Dalian 116023, China (e-mail: mengshh@dicp.ac.cn; wangjing1207@dicp.ac.cn; maoye@dicp.ac.cn).

Wuqiang Yang is with the Department of Electrical and Electronic Engineering, The University of Manchester, Manchester M13 9PL, U.K. (e-mail: w.yang@manchester.ac.uk).

This article has supplementary downloadable material available at https://doi.org/10.1109/TIM.2020.3041104, provided by the authors.

Digital Object Identifier 10.1109/TIM.2020.3041104

### I. INTRODUCTION

S A safe, economic, nonintrusive, noninvasive, and rapid response measurement technique, electrical capacitance tomography (ECT) has been used for the measurement of fluidized beds for many years [1]–[3]. ECT is based on the measurement of variation in capacitance from a multielectrode sensor, which is normally installed externally of a pipe or vessel, e.g., a fluidized bed [4]–[6]. Stable and accurate capacitance measurements are essential to high-quality images. In ECT, measurement errors are caused by many possible sources, such as noise from equipment, powerlines, and electrification, the change in temperature and humidity, and the inaccurate fabrication of an ECT sensor [7]–[9].

In the past few years, researchers made effort on 3-D ECT. Compared with 2-D ECT, it is expected that 3-D ECT can provide more measurements and, hence, more information from the volumetric images, e.g., flow pattern and size and velocity of bubbles in a fluidized bed [10]–[12]. Some researchers use an ECT sensor with electrodes in a single plane and time as the 3-D to reconstruct 3-D images [13], [14]. The condition for this approach to work is that the flow velocity must be constant, and it faces an axial average effect, which causes distortion of the reconstructed 3-D images [15], [16]. In principle, multiplane electrodes are preferred for 3-D ECT [15]. Usually, three or four planes of rectangular electrodes are arranged inline [17]-[19]. In this case, the measured signals between the electrodes in different planes, which are far away from each other and much smaller than those between electrodes in the same plane, causing serious measurement errors [20]–[22].

The ill-posedness of the inverse problem is reflected by the condition number of the sensitivity matrix. Because 3-D ECT provides many more independent measurements, the condition number is much larger than 2-D ECT, and hence, the calculated permittivity distribution, i.e., the reconstructed 3-D image, is more sensitive to measurement errors than 2-D ECT [23]. In other words, 3-D ECT is much more difficult than 2-D ECT both in capacitance measurement and image reconstruction (IR) [20]. Therefore, the measurement error is a serious challenge for 3-D ECT and makes it difficult to obtain high-quality 3-D images [7].

As mentioned earlier, one of the challenges of 3-D ECT is that the signals between the electrodes from layers far from each other are extremely weak, which could be readily affected by noise and cause large-signal disturbance on the measurements. The small-signal disturbance is critical for

1557-9662 © 2020 IEEE. Personal use is permitted, but republication/redistribution requires IEEE permission. See https://www.ieee.org/publications/rights/index.html for more information.

obtaining high image quality for the measurement of moving objects, e.g., gas bubbles in fluidized beds. Indeed, some work on 3-D ECT has been conducted. In addition to the well-known ill-posed inverse problems [15], [24], [25] in IR, optimal design of 3-D ECT sensors also received attention, e.g., the number of electrodes in different planes [26], the angular distribution of electrodes [27]–[29], and the electrode length [22]. Ye et al. [26] studied three 3-D ECT sensors with three planes of rectangular electrodes in each sensor and four, eight, and 12 electrodes in each plane. They found that the inverse problem becomes more ill-conditioned and more susceptible to noise with the increase in the number of electrodes. They suggested that four electrodes in each plane are used with a signal-to-noise ratio (SNR) of less than 50. Rotation of electrodes in different planes can improve the homogeneity and decrease the condition number of sensitivity matrix although the image quality becomes slightly worse [27], [28]. By rotating an electrode plane by 45° while keeping adjacent planes at the same position, Wang et al. [29] studied the staggered electrodes. They compared two ECT sensors, i.e., three planes with four electrodes in each plane and four planes with six electrodes in each plane, and found that the latter can provide higher spatial resolution for reconstructed 3-D images. However, to ensure the reliability of measured signals, a reduced sampling frequency was used. Li and Holland [22] studied a 3-D ECT sensor with four planes of rectangular electrodes and six electrodes in each plane. They discussed the effect of different electrode length on the image quality and showed that shorter electrodes result in a smaller condition number of sensitivity matrix and higher image quality. They recommended the electrode length is 1.5 times the pipe diameter. Up until now, however, improving the quality of measured signals via optimization of electrodes is yet to be studied, especially with regard to the applications of 3-D ECT in measuring moving objects [7].

Soleimani et al. [15] investigated a true 3-D ECT sensor with electrodes in six sides of a cube to reconstruct 3-D images directly. Because they used rectangle electrodes with sharp corners, the electric charges are readily accumulated on the corners, causing a significant fringe effect. An ECT sensor with hexagon electrodes was proposed and compared with the ECT sensor with rectangular electrodes by numerical simulation, showing that the former can provide a more uniform sensitivity distribution along the axial direction [30]. However, no experimental evidence was shown to confirm the performance of the ECT sensor with hexagon electrodes. Baidillah et al. [31] considered ECT sensors with regular square, triangular, trapezoidal, and hexagonal electrodes. They compared the performance of ECT sensors in terms of capacitance data, sensitivity map, and image quality in the tests of static models. However, they did not consider the effect of electrode shape on measurements of moving objects.

In this article, we will identify the optimal sensor design by comparing the standard deviation of measured signals and imaging quality for different 3-D ECT sensors. We also focus on the measurement of moving objects, in which small-signal disturbance is critical for obtaining high-quality images.

### II. PRINCIPLE OF 3-D ECT

An ECT system mainly consists of a multielectrode sensor, sensing electronics, and a computer for hardware control and IR, as shown in Fig. S1 in the Supplementary Material. An ECT sensor with a number of electrodes is used to measure variation in capacitance caused by different permittivity and/or different permittivity distributions. The relationship between capacitance and permittivity is given by

$$C_{i,j} = -\frac{1}{V} \oint_{\Gamma} \varepsilon(x, y, z) \nabla \varphi(x, y, z) \cdot d\Gamma$$
 (1)

where  $C_{i,j}$  is the capacitance between the excitation electrode i and the detection electrode j, V is the potential difference,  $\Gamma$  is the surface of electrodes,  $\varepsilon(x, y, z)$  is the permittivity distribution, and  $\varphi(x, y, z)$  is the potential distribution.

It is difficult to calculate the capacitance value for a 3-D ECT sensor because of the complicated relative position of the excitation electrode(s) and detection electrodes in the sensing space, which causes divergence and bending of electric field lines. Therefore, a numerical simulation based on a finite-element method (FEM), e.g., COMSOL Multiphysics, is often used to calculate capacitance.

Because (1) is too complicated, its linearized normalization form is usually expressed as [32]

$$\lambda = Sg. \tag{2}$$

This is a matrix equation, where  $\lambda$ , S, and g are the normalized capacitance vector, normalized sensitivity matrix, and the normalized permittivity vector, respectively. It is not necessary to obtain the absolute capacitance for IR. Equation (2) is the first-order approximation of (1), which introduces linearization error. Because the linearization error is small, it is always neglected.

The sensitivity matrix S is an  $M \times N$  matrix, where M is the number of the capacitance measurements, and N is the number of voxels. Yang and Conway [33] obtained a sensitivity distribution by physically measuring the sensitivity to a test rod. They found that the sensitivity distribution obtained is similar to that calculated by numerical simulation. Because the physical measurement is very demanding in positioning the test rod, it is difficult to implement this approach with many voxels for 3-D ECT. Therefore, numerical simulation is used to calculate the sensitivity matrix, based on FEM. The following is the equation used [34]–[36]:

$$S_{i,j}^*(k) = -\int_{v(k)} \frac{E_i(k)}{V_i} \cdot \frac{E_j(k)}{V_j} dv$$
 (3)

where  $E_i(k)$  is the electric field distribution of the kth element when the ith electrode is applied voltage  $V_i$ , the same with  $E_i(k)$ , and v(k) is the volume of the voxel k.

The normalized form of S is

$$S_{i,j}(k) = \frac{S_{i,j}^*(k)}{\sum_{k=1}^N S_{i,j}^*(k)}.$$
 (4)

Because M is significantly less than N, the inverse of S does not exist, which makes it impossible to obtain g in (2) directly. The 3-D regularized sensitivity distributions between

the region of excitation electrodes and detection electrodes are obviously larger than other regions. The sensitivity distribution is shown in Fig. S2 in the Supplementary Material.

Liner back projection (LBP) and Landweber iteration are the two most commonly used IR algorithms to obtain an approximate solution  $\hat{g}$ . As the simplest and fastest IR method, LBP is to replace the inverse with the transpose of S. LBP is commonly used for on-line IR, which is shown in the following equation:

$$\hat{\mathbf{g}} = \frac{\mathbf{S}^T \boldsymbol{\lambda}}{\mathbf{S}^T \boldsymbol{u}_{\boldsymbol{\lambda}}} \quad \boldsymbol{u}_{\boldsymbol{\lambda}} = [1, 1, \dots, 1]. \tag{5}$$

Because the image quality of LBP is poor, LBP can be used for qualitative analysis only. The Landweber iteration is the most widely used iterative method [37], which is based on the steepest gradient descent theory. It takes a long time to calculate but can improve image quality. The Landweber iteration is often used for off-line quantitative analysis and expressed by the following equation:

$$\hat{\mathbf{g}}_{k+1} = \hat{\mathbf{g}}_k - \alpha \mathbf{S}^T (\mathbf{S} \hat{\mathbf{g}}_k - \lambda). \tag{6}$$

A projected operator of the Landweber iteration can be used to improve its convergence, which is expressed by

$$\hat{\boldsymbol{g}}_{k+1} = P[\hat{\boldsymbol{g}}_k - \alpha \boldsymbol{S}^T (\boldsymbol{S} \hat{\boldsymbol{g}}_k - \boldsymbol{\lambda})] \tag{7}$$

$$P[f(x)] = \begin{cases} 0 & \text{if } f(x) < 0\\ f(x) & \text{if } 0 \le f(x) \le 1\\ 1 & \text{if } f(x) > 1. \end{cases}$$
 (8)

Choosing relaxation factor  $\alpha$  and the number of iterations is empirical, e.g., the number of iterations is often chosen as a few hundred.  $\alpha$  is positive, which decides the step at each iteration, and it can be changed in the iteration process or chosen as a fixed value for simplification [23], [32].

# III. NUMERICAL SIMULATION AND EXPERIMENT

### A. Experimental Conditions

High SNR sensing electronics is essential to the accurate measurement for 3-D ECT because a 3-D ECT sensor has much small capacitance than a 2-D ECT sensor, and hence, the measurement errors cause a more serious problem, especially for the measurements between electrodes in different planes that are far away from each other. SNR is calculated by the following equation for ECT:

$$SNR = 20\log_{10} \sqrt{\frac{\sum_{i=1}^{F} C_i^2}{\sum_{i=1}^{F} (C_i - \bar{C}_i)^2}}$$
 (9)

where  $c_i$  is the *i*th group of measurement capacitance signals between electrode pairs,  $\bar{C}_i$  is the average measurement capacitance of the electrode pairs, and F is the number of sampling, e.g., 1000 in this work.

In Sections IV and V, SNR means the average SNR over all the electrode pairs, and the number of electrode pairs in this work is 224, as shown in Section III-C. An ac-based ECT system [8], [38] is used for capacitance measurement, which has been widely used in studying gas/solids fluidized beds [39], [40]. COMSOL Multiphysics [22], [26] is chosen for numerical simulation.

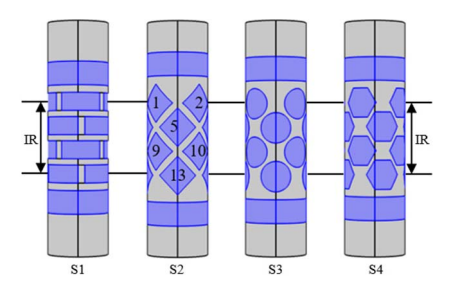


Fig. 1. 3-D ECT sensors with different shapes of electrodes. (S1) Rectangle. (S2) Diamond. (S3) Circular. (S4) Hexagon.

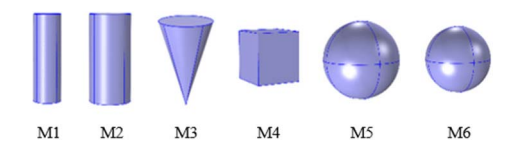


Fig. 2. Geometry of test models. (M1) Cylinder: r = 10 and L = 60. (M2) Cylinder: r = 15 and L = 60. (M3) Cone: r = 20 and h = 60. (M4) Cube: L = 30. (M5) Sphere: r = 20. (M6) Sphere: r = 15 [unit: millimeters].

# B. Sensors Design

The sensor design makes a great impact on the performance of a 3-D ECT system. For a 3-D ECT sensor, the value of measured capacitance mainly depends on the size of the electrodes, the distance between the excitation electrode and detection electrode, and their relative position. In this work, 3-D ECT sensors with staggered electrodes of different shapes, including diamond, circular, and hexagon, are compared with that with in-line rectangular electrodes (as shown in Fig. 1).

The electrodes, made of copper foil with a thickness of 0.03 mm, are mounted outside of polymethyl methacrylate tubes. The tube has an external diameter of 65 mm and a wall thickness of 2.5 mm. Each ECT sensor consists of four planes of electrodes with four electrodes in each plane. The detailed geometry parameters are shown in Fig. S3 in the Supplementary Material. The region for IR, from the center of electrodes of the bottom plane to that of the top plane, keeps the same for different ECT sensors. Two axial end screen electrodes, which have a height of 25 mm, are, respectively, installed on both ends of each ECT sensor, and an outer screen is used to cover the electrodes on the outer surface of the tube to protect the influence from external electromagnetic signals. Adjacent electrode planes are interlaced, and the distance between the first and the third plane of electrodes is obviously shortened for sensors with staggered electrodes, especially for diamond electrodes, compared with the ECT sensor with rectangular electrodes. In Fig. 1, only the electrodes on ECT sensor S2 are numbered as an example. In the four ECT sensors, the sensing region and electrode area are kept the same. However, it is difficult to maintain the same gaps between electrodes because of complex geometries for different electrode shapes. A couple of test models of different shapes made by Nylon are used for calibration and testing in the experiment. The relative permittivities of the tube, test models, and surroundings are 2, 3, and 1, respectively. Fig. 2 shows different test models and their main geometric parameters.

For the experiment, an automatic control system [13] has been developed to move test models and control the relative position and moving velocity of the test models. A thin bamboo stick was specially made to link the test models at one end and fixed at a holding part, which can freely move in 3-D. Thus, the starting/ending position and moving velocity can be controlled precisely by adjusting the controlling parameters.

# C. Data Acquisition

Dual-electrode excitation is used to increase the magnitude of measurement capacitance. For instance, when two adjacent electrodes (say, 1 and 2) are applied for excitation, the rest of the electrodes (say, 3–16) are used for detection in turn in sequence. There are totally  $16 \times 14 = 224$  measured data in each group of capacitance measurements. The excitation signal used is sinusoidal signals with an amplitude of  $20 \ V_{p-p}$  and a frequency of  $180 \ kHz$ .

## D. Image Reconstruction

The spatial resolution used for IR is  $20 \times 20 \times 26$  in the sensing region with the volume for each voxel of 3 mm  $\times$  3 mm  $\times$  3 mm. The spatial resolution for 3-D ECT is low because of the limited number of electrodes and, hence, the limited number of independent capacitance measurements compared with the number of voxels. For the Landweber iteration, the relaxation factor is chosen as 3, and the number of iterations has been optimally selected with static experiments using different test models and used for quantitative analyze and improving the image quality. The initial value  $\hat{\mathbf{g}}_0$  is calculated by LBP. The ill-posedness of the inverse problem of 3-D ECT is very serious, which causes artifacts. Therefore, the reconstructed image needs further image processing.

Because the measurement errors cause distortion of reconstructed images, a median filter as a digital filtering technique is adopted to deal with these problems and improve the image quality. As a nonlinear smoothing filter, the median filter is to replace the noisy pixel with a median value of its surrounding voxels without concerning about the image features. The determination method of "surrounding voxels" is considered with the 3-D template of the median filter. In general, the image quality can be improved because the median filter can deal with the artifacts and distortion of images.

Image segmentation can be effectively used for extracting the boundaries of two materials with different permittivities in ECT. In this work, it is only used for a preliminary study for IR using the measured capacitance of static models because the threshold chosen for image segmentation in ECT is still an open question, and it is difficult to determine the threshold for complex models in measurements, e.g., bubbles in a fluidized bed. However, the scope of this article is to discuss the design of 3-D ECT sensors, we are not going to discuss the threshold selection, and thus, the Otsu method has not been used for moving objects. A 3-D template of the median filter used is shown in Fig. 3, where the number "1" means the voxel is considered and "0" means ignored.

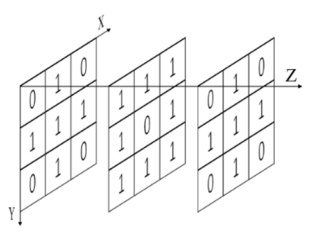


Fig. 3. 3-D template of the median filter.

### E. Evaluation Criteria

Standard deviation (STD) is used to evaluate the disturbance of the measured signals and the uniformity of sensitivity distribution, and image error ( $I_e$ ) and correlation coefficient ( $C_c$ ) are used for comparison of the image quality. The condition number (CN) of a sensitivity matrix is used to assess the ill-posedness, which reflects the sensitivity of the solution of the inverse problem to the measurement errors. The following are definitions for STD,  $I_e$ ,  $C_c$ , and CN:

STD = 
$$\sqrt{\frac{1}{N-1} \sum_{i=1}^{N} (C_i - \overline{C})^2}$$
 (10)

$$STD = \sqrt{\frac{1}{MN - 1} \sum_{l=1}^{M} \sum_{k=1}^{N} (S_{l \cdot k} - \bar{S})^2}$$
 (11)

$$I_e = \frac{\|\hat{\mathbf{g}} - g\|}{\|g\|} \tag{12}$$

$$C_c = \frac{\sum_{i=1}^{N} (\hat{g}_i - \bar{g})(g_i - \bar{g})}{\sqrt{\sum_{i=1}^{N} (\hat{g}_i - \bar{g})^2 \sum_{i=1}^{N} (g_i - \bar{g})^2}}$$
(13)

$$CN = \sqrt{\frac{\lambda_1}{\lambda_n}} \tag{14}$$

where  $\lambda_1$  and  $\lambda_n$  are the maximum and minimum eigenvalues of the sensitivity matrix.

# IV. RESULTS AND DISCUSSION

### A. Capacitance Data

Fig. 4 shows the numerical simulation results of comparison of capacitance data from ECT sensors S1, S2, S3, and S4 when the ECT sensors are filled with low permittivity material, while electrodes 1 and 2 used for excitation and electrodes in the third and fourth planes used for detection. The capacitance values of the 3-D ECT sensors with staggered electrodes are bigger than those with rectangular electrodes, e.g., the minimum capacitances of the four ECT sensors are 0.88, 1.07, 0.98, and 1.05 fF, respectively, which is favorable for improvement of the precision of the measured signals.

To further illustrate the effects of electrode shape and arrangement, simulation is carried out on the 3-D ECT sensors with hexagonal electrodes of different edge length (L), which results in varying electrode area, and the capacitance data are compared when the ECT sensors are filled with low permittivity materials. The results are shown in Table SI in the Supplementary Material. With the decrease in L, the capacitance between the electrode pairs shows an apparent

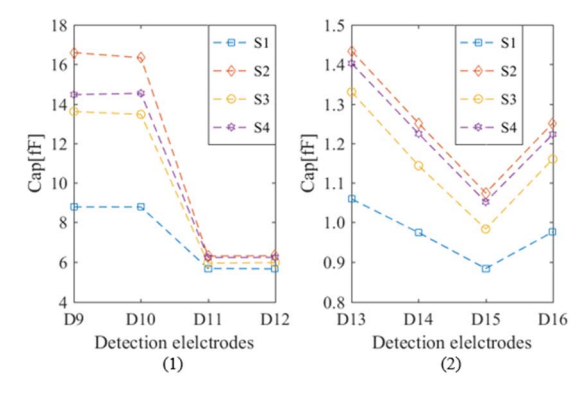


Fig. 4. Comparison of capacitance data of ECT sensors S1, S2, S3, and S4 when the ECT sensors are filled with low permittivity material, electrodes 1 and 2 were used for excitation, (1) electrodes in the third planes (from D9 to D12) are used for detection, and (2) electrodes in the fourth planes (from D12 to D16) are used for detection. Note that D9 means electrode number 9 is used as the detection electrode.

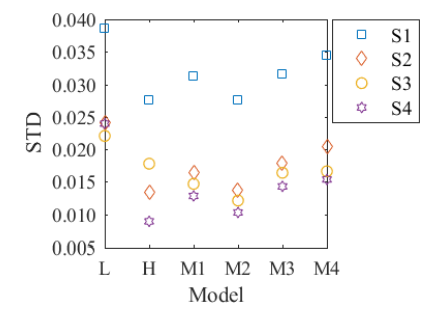


Fig. 5. Average STD of 1000 groups of data for 224 measured normalized capacitance signals using 3-D ECT sensors in different testing conditions. The data were obtained by experiment.

reduction, which, in turn, leads to an increment in errors that are unfavorable for the measurements. Therefore, an electrode length of 17.9 mm is used in this study.

Experiments were conducted for the following situations: 1) the tube was filled with low permittivity material ("L" in Fig. 5); 2) the tube was filled with high permittivity material ("H" in Fig. 5); and 3) test models of M1, M2, M3, and M4 in the tube.

Air was used as the low permittivity material and Nylon for test models and as high permittivity materials. The average STD represents the overall disturbance of measured signals from the ECT sensors. STD of the measured signals is closely related to the design of 3-D ECT sensors, and the disturbance of the measured signals of the 3-D ECT sensors with staggered electrodes is obviously lower than those with rectangular electrodes, according to STD of the measured signals. Especially, ECT sensor S4 with hexagon electrodes is superior to ECT sensors S2 and S3 with diamond and circular electrodes. When a 3-D ECT sensor is filled with low permittivity material, the performance is poor because of weak measured signals. The disturbance of measured signals is significantly reduced when a high permittivity object is located in the measurement region.

# B. Electric Field Distribution

For an ECT sensor, the arrangement of electrodes would affect the electric field distribution. For instance, the electric charges would readily accumulate at the edge and, especially,

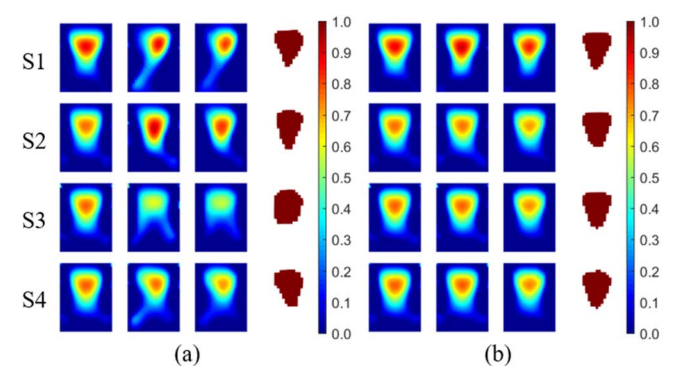


Fig. 6. Reconstructed images of M3 of different 3-D ECT sensors with noise data by numerical simulation. (a) SNR = 45. (b) SNR = 60. The images shown in the first column are reconstructed using noise-free data, the images shown in the second column are based on the Gaussian white noise data with SNR of 45 or 60 dB, the images shown in the third column are processed by the median filter, and the images shown in the fourth column are further processed with Otsu's method to extract the boundaries of objects.

the corner of electrodes, which can cause the "soft-field" effect and, thus, nonlinear and nonuniform distribution of the sensitivity. In this sense, a more uniform distribution of electric field is favorable in 3-D ECT measurements. Fig. S4 in the Supplementary Material shows the electric field intensity distribution of the four 3-D ECT sensors. Fig. S4 in the Supplementary Material displays the electric field distribution to qualitatively illustrate the influence of electrode shapes and arrangement, partially explaining the underlying mechanism of nonlinear, and nonuniform distribution of the sensitivity shown in Section IV-C.

### C. Sensitivity Field

Table SII in the Supplementary Material gives STD and CN of normalized sensitivity distribution when the 3-D ECT sensors are filled with low permittivity material. STD indicates the uniformity of the sensitivity distribution [20], [22], and CN reflects the ill-posedness of the inverse problem or the change in calculated permittivity distribution for a small change in measured signals. The smaller the values of STD and CN are, the more uniform the sensitivity is, and the less ill-posedness the inverse problem is. The data reveal that the uniformity of the sensitivity of ECT sensors S2, S3, and S4 is slightly higher than ECT sensor S1, and the ill-posedness of the inverse problem of ECT sensors S2 and S1 is slightly superior to ECT sensors S3 and S4. In addition, the normalized sensitivity distribution in the axial direction for the 3-D ECT sensors is considered, as shown in Fig. S5 in the Supplementary Material, which reflects that ECT sensor with rectangular electrodes somehow has "dead zones" [20] at the end of the ECT sensor, whereas ECT sensors with staggered electrodes have no obvious "dead zones" in the sensing regions.

### D. Experiment With Static Test Models

Fig. 6 and Fig. S6 in the Supplementary Material show the reconstructed 3-D isosurface images of M3 and M5 with numerical simulation data. The test models are located in the center of the tube. Images in the first column are reconstructed using noise-free data, and the second column is based on the

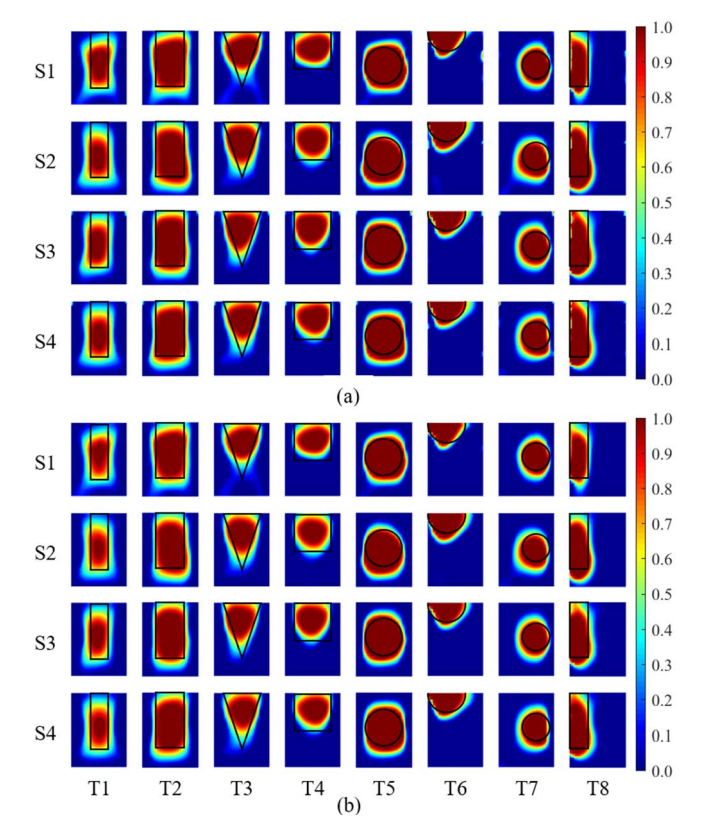


Fig. 7. Reconstructed images of static test models using 3-D ECT sensors with experiments. (a) Original images. (b) Images processed with the median filter.

Gaussian white noise data with an SNR of 45 or 60 dB. It can be seen from the first two columns that artifacts clearly exist, even with noise-free data, and adding noise makes a little effect on artifacts. The primary reason for artifacts is the ill-posedness of the inverse problems. In addition, image distortion becomes more serious with an SNR of 45 dB than 60 dB. A median filter is used to process the reconstructed images that are displayed in the third column of Fig. 6 and Fig. S6 in the Supplementary Material. A comparison of quality between the reconstructed images processed with the median filter and original images confirms that the median filter can significantly improve the image quality. Images in the fourth column are further processed with Otsu's method [41] to extract the boundaries of objects. Otsu's method, an image segmentation method based on maximizing the object function, is used for automatically obtaining an optimal threshold from the gray histogram of reconstructed images. This is an attempt to adaptively obtain the boundaries of reconstructed images with threshold segmentation, e.g., bubbles in fluidized beds. Clear and accurate boundaries are helpful for the analysis of flow patterns and the gas velocity of fluidized beds [42].

Fig. 7 shows the reconstructed images of static test models with average measured signals of 1000 groups by experiments, where Fig. 7(a) shows the original images without filtering and Fig. 7(b) shows the original images processed with the median filter. Reconstructed images of (T3) and (T5) in Fig. 7 are compared with the simulation results. The reason for the difference of reconstructed images between simulation and experiment may be that the measured signals in the experiment

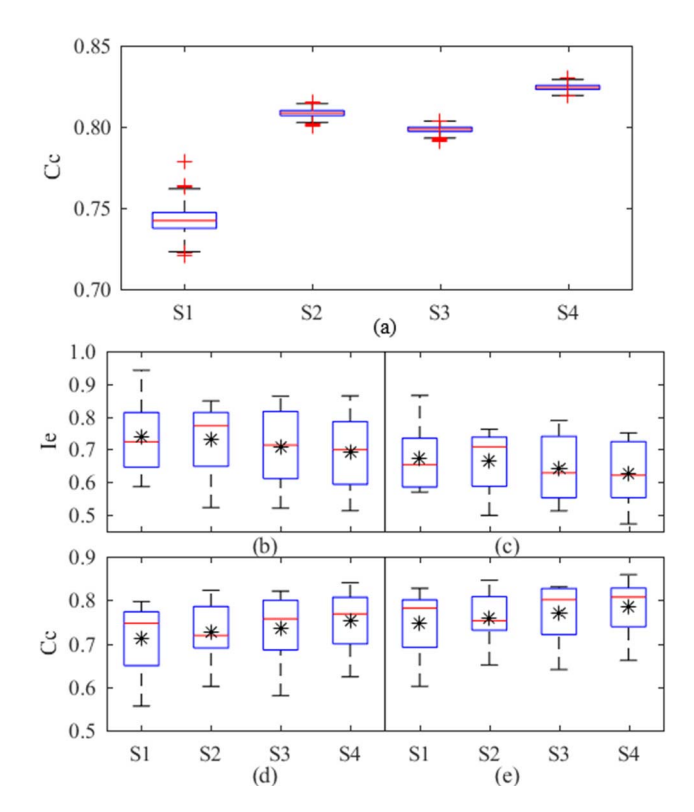


Fig. 8. Evaluation of image quality with 3-D ECT sensors by experiment. (a)  $C_c$  of M2 with 1000 groups of measured signals. (b)  $I_e$  without a median filter. (c)  $I_e$  with a median filter. (d)  $C_c$  without a median filter. (e)  $C_c$  with the median filter.

are preliminarily processed. In general, the quality of images reconstructed by measured capacitance in the experiment is higher than that in simulation with an SNR of 45. The experimental results confirm the conclusion from the simulation that the image quality is improved after an image is processed by the median filter. Image segmentation is not adopted in the experiment because the selection for threshold in complicated measurement conditions remains an open question and needs further study.

The 3-D shape of the test models can be obtained from the reconstructed images with a 3-D ECT sensor, especially when reconstructed images are processed by the median filter. Artifacts of images obtained from the four 3-D ECT sensors clearly exist, but image distortion with 3-D ECT sensors with staggered electrodes is smaller than that with rectangular electrodes. From the reconstructed images of *M*4 compared with other test models, it can be conjectured that the reconstructed images of test models with sharp edges are not very well resolved with 3-D ECT.

Fig. 8 shows the quantitative analysis of image quality of test models in different experiment conditions, and the detailed data were shown in Table SIII in the Supplementary Material, which confirms the result of Fig. 7. The number of iterations used for the Landweber iteration is optimal from 100 to 1000 to obtain the lowest  $I_e$  and highest  $C_c$  for different test models and different ECT sensors. The optimal process is shown in Table SIV in the Supplementary Material in which model M2 is chosen as an example to show the variation of  $I_e$  and  $C_c$  with different numbers of iterations. When the

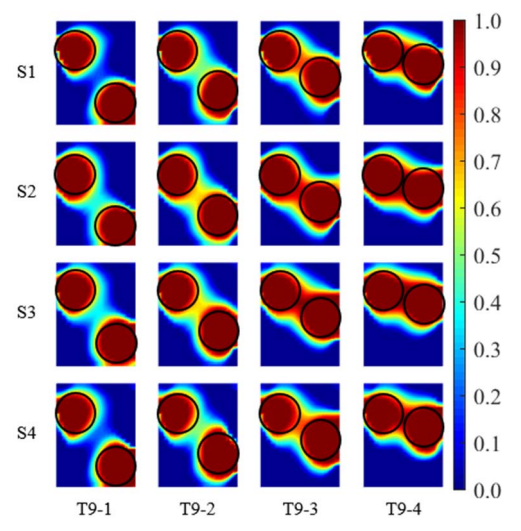


Fig. 9. Reconstructed images by a combination of two M6 using 3-D ECT sensors with experiment.

number of iterations is greater than 300, it has little effect on  $I_e$  and  $C_c$  but needs longer computing time. Therefore, in the following section, 300 is chosen as the fixed number of iterations for the Landweber iteration. The results of reconstructed 3-D images of test models indicate that a 3-D ECT sensor with 16 electrodes in four planes can maintain a good SNR and provide high image quality.

For measuring a moving object, e.g., gas bubbles in a fluidized bed, the measurement is unrepeatable, and small-signal disturbance is critical for obtaining high image quality. Let us take the results of  $C_c$  of the reconstructed images of M2 with 1000 groups of measured signals as an example. As shown in Fig. 8(a), the ECT sensors with staggered electrodes can provide more stable measurement signals than that with rectangular electrodes, which is very important for measuring moving and dynamic objects. Fig. 8(b)–(d) shows the boxplot of quantitative analysis of image quality by measuring different static models and using the average capacitance of 1000 repeated measurements, and the reconstructed images are shown in Fig. 7. The evaluation of the reconstructed images without the median filter is shown in Fig. 8(b) and (c), while the evaluation with the median filter is shown in Fig. 8(d) and (e). The sign "\*" in Fig. 8(b)-(e) means the average evaluation result with eight measuring conditions. Basically, random errors can be minimized by measuring static models and using the average capacitance of many repeated measurements. The quality of reconstructed images by ECT sensors with staggered electrodes is better than that with rectangular electrodes, as indicated by a lower average  $I_e$ and higher average  $C_c$  on average with the average measuring signals. For example, the average  $I_e$  decreases from 0.74 to 0.69, and the average  $C_c$  increases from 0.71 to 0.75 by the ECT sensor with hexagon electrodes compared with rectangular electrodes without image process. By postprocessing with the median filter, the image quality increases as the average  $I_e$  decreases from 0.69 to 0.63, and the average  $C_c$  increases from 0.75 to 0.78 by the ECT sensor with hexagon electrodes.

Fig. 9 shows the reconstructed images of two M6 with a relative distance of 20, 12.4, 6.1, and 1.6 mm, respectively,

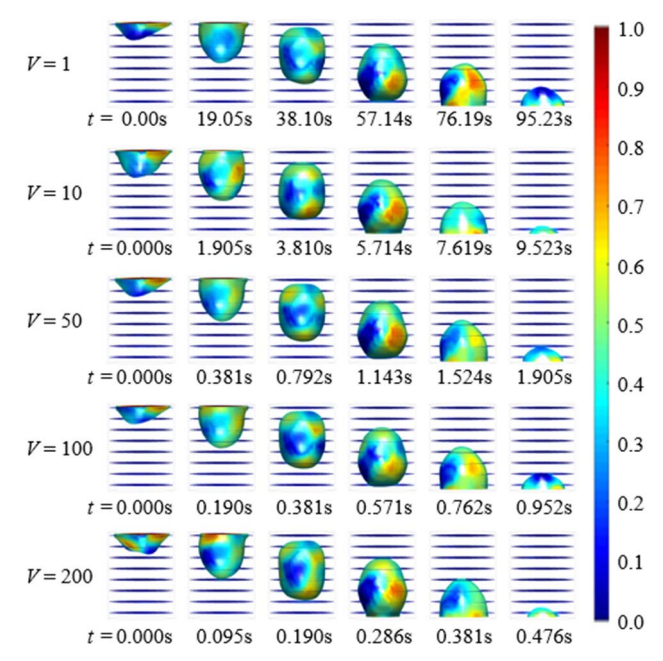


Fig. 10. Reconstructed images of the movement of M5 in different velocities using 3-D ECT sensor with hexagonal electrodes [unit: mm/s].

after postprocessing by the median filter. Fig. 9 exhibits the images when one *M*6 gradually approaches another *M*6 model. For large distances (i.e., the distance of 20 and 12.4 mm), all the ECT sensors can distinguish these two models in the sensing region. However, when the distance becomes 1.6 mm, the two models cannot be distinguished because of the "soft field" effect and low spatial resolution of ECT. The reconstructed images of multimodels need further postprocessing of images for quantitative analysis.

# E. Experiment With Motion Model

Having analyzed the performance of different 3-D ECT sensors with capacitance data, measured signals, electric field distribution, sensitivity field distribution, and image quality of static models, the 3-D ECT sensor with hexagonal electrodes is chosen for further testing to confirm its performance. In an actual gas-solids two-phase flow, gas or solids phases are moving in the measurement region, and the permittivity distribution is changing, making the measurement even more difficult. Therefore, it is difficult to obtain the true distribution of gas/solids phases in a gas-solids fluidized bed to evaluate the measurement results. Because the difference between the static test model experiment and real fluid is considerable, an experiment with a motion model was conducted. In this experiment, a test model moves at a certain velocity (1, 10, 50, 100, and 200 mm/s, respectively) to simulate the real fluid flow.

Fig. 10 shows the part of the reconstructed images of M5 with different movement velocities passing through the measurement region. Six images are chosen at the same time interval to display the trajectory of the test model for each movement velocity. With the 3-D ECT sensor with hexagonal electrodes, the main shape characteristic of the test model can be obtained, confirming that the ECT sensor has a good

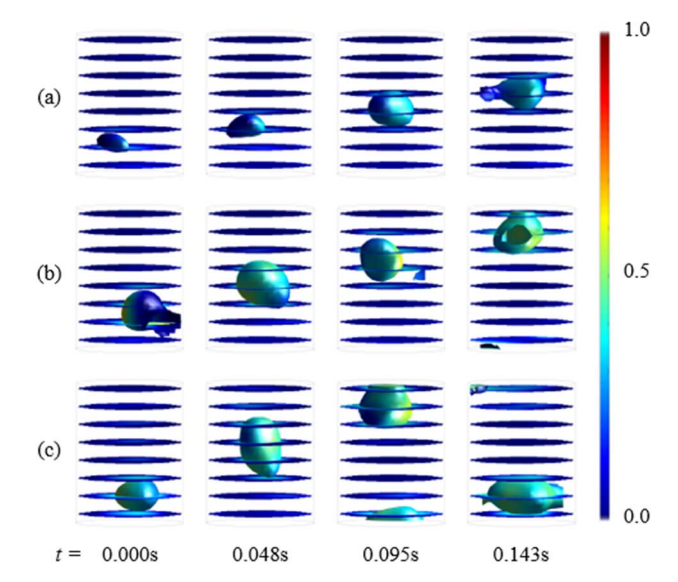


Fig. 11. Images of bubble motion at different superficial gas velocities of fluidized beds with 3-D ECT sensor with hexagonal electrodes. (a)  $U/U_{\rm mf}=1.5$ . (b)  $U/U_{\rm mf}=2.0$ . (c)  $U/U_{\rm mf}=2.5$ .

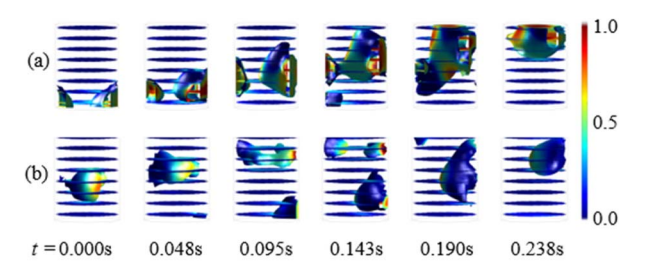


Fig. 12. Images reconstructed by sensor S4 showing bubble coalescence and break in fluidized beds. (a) Coalescence. (b) Break.

dynamic performance. When the movement velocity (V) is no more than 200 mm/s and the sampling frequency is about 21 frames/s used in this work, images of the test models passing through the sensing region can still be reconstructed with relatively good quality. When the velocity is very small, e.g., 1 or 10 mm/s, it has little effect on the quality of reconstructed images. However, when V = 200 mm/s, it has a slight movement of the test models in the sensing region in a single frame of measurement, which causes distortion of the image. If the movement velocity of the test model increases further, the distortion will be more severe. In this circumstance, the sampling frequency of ECT needs to be increased to obtain reliable measured signals and good image quality. Further image processing can be performed to obtain more information, such as the central position, volume, and velocity of the test model. However, this work is focused on the performance of 3-D ECT sensors, and further image processing will be the topic for future research.

# F. Application in Fluidized Beds

The particles used for the fluidized bed experiment are  $Al_2O_3$  (diameter  $d_p = 500~\mu m$  with a uniform size distribution, bulk density  $\rho_b = 1.09~g/cm^3$ , and the minimum fluidized velocity  $U_{\rm mf} = 7.0~cm/s$  with air at ambient temperature and pressures). Fig. 11 shows the reconstructed images of bubble motion when the superficial gas velocity

is  $U/U_{\rm mf}=1.5, 2.0$ , and 2.5. The position and size of bubbles can be observed clearly from the 3-D images. With an increase in superficial gas velocity, the size, velocity, and frequency of bubbles increase. The bubbles coalescence and break can be observed by 3-D ECT, as shown in Fig. 12. The reconstructed 3-D images need further processing to obtain more quantitative information about the flow characteristics in fluidized beds, such as the velocity, frequency, and size of bubbles.

# V. CONCLUSION

In this work, we studied 3-D ECT sensors with different arrangements and different shapes of electrodes, including staggered diamond, circular, and hexagon electrodes and in-line rectangular electrodes, and the effect of arrangement and shape of electrodes on the measured capacitance signals and image quality. The results show that 3-D ECT sensors with staggered electrodes can decrease the disturbance of measured signals by increasing the capacitance between electrodes in different planes far away from each other, thus making it easier to measure capacitance. It is confirmed by a static test using models for the experiment and comparison of STD from the measured signals of different 3-D ECT sensors. In addition, the quality of images generated by the 3-D ECT sensor with staggered electrodes is superior to that with rectangular electrodes. The 3-D ECT sensor with 16 electrodes in four planes can maintain good SNR and image quality with a suitable sensor design. The quality of images processed by the median filter is obviously improved. The electric field distribution and fringe effect of 3-D ECT sensors with different shapes of electrodes are also discussed.

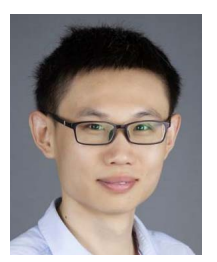
Having analyzed the performance of different 3-D ECT sensors according to measurement stability and accuracy, the 3-D ECT sensor with hexagonal electrodes is chosen for the motion test model experiment to confirm its performance. Under the condition of the high moving velocity of test models ( $U=0.2 \, \text{m/s}$ ), images of the test models can be reconstructed using the 3-D ECT sensor with hexagonal electrodes, giving relatively good quality. Finally, a fluidized bed experiment is conducted. Not only the moving trajectory of bubbles but also more complex phenomena, such as bubble coalescence and break, can be observed using the 3-D ECT sensor with hexagonal electrodes.

### REFERENCES

- C. G. Xie et al., "Electrical capacitance tomography for flow imaging: System model for development of image reconstruction algorithms and design of primary sensors," *IEE Proc. G Circuits, Devices Syst.*, vol. 139, no. 1, pp. 89–98, Feb. 1992.
- [2] S. Liu, R. Yan, H. Wang, F. Jiang, and X. Dong, "Applications of electrical capacitance tomography in two phase flow visualization," *J. Thermal Sci.*, vol. 13, no. 2, pp. 179–186, May 2004.
- [3] K. Huang et al., "High-temperature electrical capacitance tomography for gas-solid fluidised beds," Meas. Sci. Technol., vol. 29, no. 10, Oct. 2018, Art. no. 104002.
- [4] W. Yang, "Design of electrical capacitance tomography sensors," *Meas. Sci. Technol.*, vol. 21, no. 4, Apr. 2010, Art. no. 042001.
- [5] C. E. Agu, A. Ugwu, C. Pfeifer, M. Eikeland, L.-A. Tokheim, and B. M. E. Moldestad, "Investigation of bubbling behavior in deep fluidized beds at different gas velocities using electrical capacitance tomography," *Ind. Eng. Chem. Res.*, vol. 58, no. 5, pp. 2084–2098, Feb. 2019.

- [6] T. Suppan, M. Neumayer, T. Bretterklieber, and S. Puttinger, "Prior design for tomographic volume fraction estimation in pneumatic conveying systems from capacitive data," *Trans. Inst. Meas. Control*, vol. 42, no. 4, pp. 716–728, Feb. 2020.
- [7] L.-L. Gu, Y. Zhang, and J. Zhu, "Wavelet denoising and nonlinear analysis of solids concentration signal in circulating fluidized bed riser," *Particuology*, vol. 49, pp. 105–116, Apr. 2020.
- [8] W. Q. Yang and T. A. York, "New AC-based capacitance tomography system," *IEE Proc.-Sci., Meas. Technol.*, vol. 146, no. 1, pp. 47–53, Jan. 1999.
- [9] Y. Zhang, Y. C. Liang, and C.-H. Wang, "Hazard of electrostatic generation in a pneumatic conveying system: Electrostatic effects on the accuracy of electrical capacitance tomography measurements and generation of spark," *Meas. Sci. Technol.*, vol. 19, no. 1, Jan. 2008, Art. no. 015502.
- [10] R. Wajman, R. Banasiak, L. Mazurkiewicz, T. Dyakowski, and D. Sankowski, "Spatial imaging with 3D capacitance measurements," *Meas. Sci. Technol.*, vol. 17, no. 8, pp. 2113–2118, Aug. 2006.
- [11] J. M. Weber and J. S. Mei, "Bubbling fluidized bed characterization using electrical capacitance volume tomography (ECVT)," *Powder Technol.*, vol. 242, pp. 40–50, Jul. 2013.
- [12] T. C. Chandrasekera, Y. Li, D. Moody, M. A. Schnellmann, J. S. Dennis, and D. J. Holland, "Measurement of bubble sizes in fluidised beds using electrical capacitance tomography," *Chem. Eng. Sci.*, vol. 126, pp. 679–687, Apr. 2015.
- [13] J. Shen, S. Meng, M. Ye, W. Yang, and Z. Liu, "3D image reconstruction using an ECT sensor with a single layer of electrodes," *Meas. Sci. Technol.*, vol. 31, no. 8, Aug. 2020, Art. no. 085106.
- [14] B. K. Singh, S. Roy, and V. V. Buwa, "Bubbling/slugging flow behavior in a cylindrical fluidized bed: ECT measurements and two-fluid simulations," *Chem. Eng. J.*, vol. 383, Mar. 2020, Art. no. 123120.
- [15] M. Soleimani, H. Wang, Y. Li, and W. Yang, "A comparative study of 3D electrical capacitance tomography," *Int. J. Inf. Syst. Sci.*, vol. 3, no. 2, pp. 292–306, 2007.
- [16] W. Warsito, Q. Marashdeh, and L.-S. Fan, "Electrical capacitance volume tomography," *IEEE Sensors J.*, vol. 7, no. 4, pp. 525–535, Apr. 2007.
- [17] R. Banasiak, R. Wajman, D. Sankowski, and M. Soleimani, "Three-dimensional nonlinear inversion of electrical capacitance tomography data using a complete sensor model," *Prog. Electromagn. Res.*, vol. 100, pp. 219–234, 2010, doi: 10.2528/PIER09111201.
- [18] A. Wang, Q. Marashdeh, B. J. Motil, and L.-S. Fan, "Electrical capacitance volume tomography for imaging of pulsating flows in a trickle bed," *Chem. Eng. Sci.*, vol. 119, pp. 77–87, Nov. 2014.
- [19] J. M. Weber, M. M. Bobek, R. W. Breault, J. S. Mei, and L. J. Shadle, "Investigation of core-annular flow in an industrial scale circulating fluidized bed riser with electrical capacitance volume tomography (ECVT)," *Powder Technol.*, vol. 327, pp. 524–535, Mar. 2018.
- [20] Y. Li and D. J. Holland, "Fast and robust 3D electrical capacitance tomography," *Meas. Sci. Technol.*, vol. 24, no. 10, Oct. 2013, Art. no. 105406.
- [21] D. Yang, L. Liu, and W. Feng, "Experimental investigation of an internally circulating fluidized bed with 32-electrode electrical capacitance volume tomography," *Measurement*, vol. 127, pp. 227–237, Oct. 2018.
- [22] Y. Li and D. J. Holland, "Optimizing the geometry of three-dimensional electrical capacitance tomography sensors," *IEEE Sensors J.*, vol. 15, no. 3, pp. 1567–1574, Mar. 2015.
- [23] W. Q. Yang and L. Peng, "Image reconstruction algorithms for electrical capacitance tomography," *Meas. Sci. Technol.*, vol. 14, no. 1, pp. R1–R13, Jan. 2003.
- [24] A. Olmos, J. Primicia, and J. Marron, "Influence of shielding arrangement on ECT sensors," Sensors, vol. 6, no. 9, pp. 1118–1127, Sep. 2006.
- [25] F. Wang, Q. Marashdeh, L.-S. Fan, and W. Warsito, "Electrical capacitance volume tomography: Design and applications," *Sensors*, vol. 10, no. 3, pp. 1890–1917, Mar. 2010.
- [26] J. Ye, H. Wang, and W. Yang, "Characterization of a multi-plane electrical capacitance tomography sensor with different numbers of electrodes," *Meas. Sci. Technol.*, vol. 27, no. 3, Mar. 2016, Art. no. 035103.
- [27] H. Yan, S. Liu, and Y. Sun, "Comparative study on 3D capacitance imaging sensors," in *Proc. Int. Conf. Test, Meas. Comput. Methods* (TMCM), vol. 26, S. B. Kafaki, S. Wahab, and B. Kalantari, Eds. Chiang Mai, Thailand, Nov. 2015, pp. 145–148.
- [28] J. Ye, M. Mao, H. Wang, and W. Yang, "An evaluation of the rotation of electrodes in multi-plane electrical capacitance tomography sensors," *Meas. Sci. Technol.*, vol. 26, no. 12, Dec. 2015, Art. no. 125404.

- [29] A. Wang, Q. M. Marashdeh, F. L. Teixeira, and L.-S. Fan, "Electrical capacitance volume tomography: A comparison between 12- and 24-channels sensor systems," *Prog. Electromagn. Res. M*, vol. 41, pp. 73–84, 2015, doi: 10.2528/PIERM15011412.
- [30] K. Brandisky, D. Sankowski, and R. Banasiak, "Analysis and simulation of novel hexagonal electrode electrical capacitance tomography sensor," in *Proc. IET 8th Int. Conf. Comput. Electromagn. (CEM)*, 2011, pp. 148–149, doi: 10.1049/cp.2011.0077.
- [31] M. R. Baidillah, M. Mukhlisin, and W. P. Taruno, "Comparisons of sensor geometries for electrical capacitance volume tomography," *Int.* J. Innov. Comput. Inf. Control, vol. 9, no. 11, pp. 4447–4457, Nov. 2013.
- [32] L. Peng, H. Merkus, and B. Scarlett, "Using regularization methods for image reconstruction of electrical capacitance tomography," *Part. Part. Syst. Characterization*, vol. 17, no. 3, pp. 96–104, Oct. 2000.
- [33] W. Q. Yang and W. F. Conway, "Measurement of sensitivity distributions of capacitance tomography sensors," *Rev. Sci. Instrum.*, vol. 69, no. 1, pp. 233–236, Jan. 1998.
- [34] R. He, M. S. Beck, C. G. Xie, C. M. Beck, and R. C. Waterfall, "Engine flame imaging using electrical capacitance tomography," *Electron. Lett.*, vol. 30, no. 7, pp. 559–560, Mar. 1994.
- [35] Q. Marashdeh and F. L. Teixeira, "Sensitivity matrix calculation for fast 3-D electrical capacitance tomography (ECT) of flow systems," *IEEE Trans. Magn.*, vol. 40, no. 2, pp. 1204–1207, Mar. 2004.
- [36] Z. Zeeshan, F. L. Teixeira, and Q. Marashdeh, "Sensitivity map computation in adaptive electrical capacitance volume tomography with multielectrode excitations," *Electron. Lett.*, vol. 51, no. 4, pp. 334–335, Feb. 2015.
- [37] Y. Wang, H. Yan, L. Liu, and Y. Zhou, "An accelerated iterative image reconstruction algorithm based on multiple linear regression for direct 3D ECT," in *Proc. 3rd Int. Conf. Electric Electron.*, Hong Kong, Dec. 2013, pp. 480–484.
- [38] W. Q. Yang, "Further developments in an AC-based capacitance tomography system," Rev. Sci. Instrum., vol. 72, no. 10, pp. 3902–3907, Oct. 2001.
- [39] H. G. Wang, P. R. Senior, R. Mann, and W. Q. Yang, "Online measurement and control of solids moisture in fluidised bed dryers," *Chem. Eng. Sci.*, vol. 64, no. 12, pp. 2893–2902, Jun. 2009.
- [40] R. Ge, J. Ye, H. Wang, and W. Yang, "Measurement of particle concentration in a Wurster fluidized bed by electrical capacitance tomography sensors," AIChE J., vol. 60, no. 12, pp. 4051–4064, Dec. 2014.
- [41] N. Otsu, "A threshold selection method from gray-level histograms," IEEE Trans. Syst., Man, Cybern., vol. SMC-9, no. 1, pp. 62–66, Jan. 1979.
- [42] V. Agrawal, Y. H. Shinde, M. T. Shah, R. P. Utikar, V. K. Pareek, and J. B. Joshi, "Estimation of bubble properties in bubbling fluidized bed using ECVT measurements," *Ind. Eng. Chem. Res.*, vol. 57, no. 24, pp. 8319–8333, Jun. 2018.



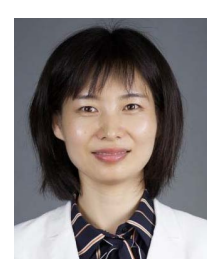
Jingjing Shen received the B.Eng. degree from Zhengzhou University, Zhengzhou, China, in 2016. He is currently pursuing the Ph.D. degree with the Dalian Institute of Chemical Physics, Chinese Academy of Sciences, Dalian, China, and also with the University of Chinese Academy of Sciences, Beijing, China.

He conducts academic research about multiphase flow measurement and simulation based on 3-D electrical capacitance tomography (ECT) technology.



**Shuanghe Meng** received the B.Eng. degree from the Dalian University of Technology, Dalian, China, in 1984.

From 1984 to 1986, she was an Assistant Engineer with Dandong Ray Instrument Industry Corporation, Dandong, China. She joined the Dalian Institute of Chemical Physics, Dalian, as an Assistant Engineer, in 1986, and as an Engineer, in 1989, where she has been a Senior Engineer, since 1999. Her research interests include electrical capacitance tomography (ECT) technology and its application in industry and thermochemistry.



**Jing Wang** received the B.Eng. and M.Eng. degrees from Xi'an Shiyou University, Xi'an, China, in 2006 and 2009, respectively.

From 2019 to 2011, she was an Assistant Engineer with the Dalian Institute of Chemical Physics, Dalian, China, where she has been an Engineer, since 2011. Her current research interests include scale-up and development of the catalytic process.



**Wuqiang Yang** (Fellow, IEEE) received the B.Eng., M.Sc., and Ph.D. degrees from Tsinghua University, Beijing, China, in 1982, 1985, and 1988, respectively.

After three years as a Lecturer with Tsinghua University, he joined The University of Manchester, Manchester, U.K., in 1991, where he has been a Professor of electronic instrumentation, since 2005. He has authored or coauthored over 400 articles. He has been invited by many universities, research institutions, companies, and international

conferences worldwide to give lectures, seminars, and keynotes. His research interests are electrical capacitance tomography (ECT) and its industrial applications.

Dr. Yang is a fellow of the IET and the Institute of Measurement and Control. He is currently an Associate Editor of the IEEE TRANSACTIONS ON INSTRUMENTATION AND MEASUREMENT and IET Science, Measurement & Technology, an Editorial Board Member of six other journals, including Measurement Science and Technology, and a Guest Editor of more than ten journal special issues. He was a Distinguished Lecturer of the IEEE Instrumentation and Measurement Society from 2010 to 2016. Since 2002, he has been in Who's Who in the World.



Mao Ye received the B.Eng. degree from the Jiangsu University of Science and Technology, Zhenjiang, China, in 1994, and the M.Eng. and Ph.D. degrees from Southeast University, Nanjing, China, in 1997 and 2000, respectively.

From 2000 to 2006, he was a Research Fellow with the University of Twente, Enschede, The Netherlands, and also with the Eindhoven University of Technology, Eindhoven, The Netherlands. From 2009 to 2010, he was an FCC Process Engineer with Shell Global Solutions International B.V.,

Amsterdam, The Netherlands. Since 2010, he has been a Professor with the Dalian Institute of Chemical Physics, Chinese Academy of Sciences, Dalian, China. He has authored more than 80 articles and has filed more than 140 patents. His current research interests include multiphase catalytic processes, measurement and simulation of multiphase flows, and industrial fluidized bed reactors.